# Peroxidase-mimicking nanozyme with surface-dispersed Pt atoms as the label for the lateral flow immunoassay of C-reactive protein

*Vasily G. Panferov, Nadezhda A. Byzova, Anatoly V. Zherdev, Boris B. Dzantiev\**

A.N. Bach Institute of Biochemistry, Federal Research Centre "Fundamentals of Biotechnology" of the Russian Academy of Sciences, Leninsky prospect 33, 119071 Moscow, Russia

**ABSTRACT**

Platinum-containing nanozymes with peroxidase-mimicking activity (PMA) have found a broad application in bioanalytical methods and are potentially able to compete with enzymes as the labels. However, traditionally used methods for the synthesis of nanozymes result in only a small fraction of surface-exposed Pt atoms, which participate in catalysis. To overcome this limitation, we propose a new approach for the synthesis of nanozymes with the efficient dispersion of Pt atoms on particles' surfaces. The synthesis of nanozymes includes 3 steps: the synthesis of gold nanoparticles

1

(Au NPs), the overgrowth of a silver layer over Au NPs (Au@Ag NPs, 6 types of NPs with different thicknesses of Ag shell), and the galvanic replacement of silver with $PtCl_6^{2-}$ leading to the formation of trimetallic Au@Ag–Pt NPs with uniformly deposited catalytic sites and high Pt-utilization efficiency. Au@Ag–Pt NPs (23 types of NPs with different concentrations of Pt) with various sizes, morphology, optical properties, and PMA were synthesized and comparatively tested. Au NPs, Au@Ag NPs, and selected Au@Ag–Pt NPs were conjugated with monoclonal antibodies and used as the labels in lateral flow immunoassay of the inflammation biomarker: C-reactive protein (CRP). The signal enhancement was achieved by the oxidation of 3,3'-diaminobenzidine by $H_2O_2$ catalyzed by Au@Ag–Pt NPs directly on the test strip. The use of Au@Ag–Pt NPs as the catalytic label produces a 65-fold lower limit of CRP detection in the serum (15 pg mL$^{-1}$) compared with Au NPs and retains all the benefits of lateral flow assay as a point-of-care method.

## 1. Introduction

Nanoparticles (NPs) with enzyme-mimicking activities (nanozymes) consisting of noble metals have found a broad application as the signal-generator label in different assays.[1] Among them, platinum-containing nanozymes demonstrate high peroxidase- and catalase-mimicking activities and remarkable stability in extremal ranges of pH, temperatures, and concentrations of inhibitors. [2,3] The combination of these features with unique physicochemical properties arising from nanoscale size and chemical composition (i.e., the high surface area for conjugation with receptor biomolecules, high molar extinction coefficient) makes Pt-containing nanozymes a promising alternative to natural peroxidases as well as a multifunctional analytical tool.[4]

However, the high consumption of precise Pt precursors for the synthesis of nanozymes remains a significant limiting factor for routine use. Thus, the new approaches for the synthesis of nanomaterials with high catalytic activity and low precursor consumption are in great demand.[5] Conventional methods of Pt-nanozyme synthesis (reduction of precursor or layer-by-layer growth) lead to the formation of NPs in which the major number of atoms are buried inside the particle and do not participate in catalysis [6] (i.e., calculations show that for 20 nm spherical Au NPs, only about 5% of all atoms are surface-exposed).[7] The exposure of a maximal number of Pt atoms on the NP's surface will facilitate high peroxidase-mimicking activity (PMA) and low consumption of the precious precursor.

At the moment, there are few approaches to synthesizing nanozymes with high PMA and low consumption of Pt precursors: the reduction of the nanozymes' sizes to the structures consisting of dozens of metal atoms (nanoclusters) [8], the formation of hollow nanoparticles [9], and the formation of close-to-monolayer catalytic-active sites [10] or even atomic dispersion of active sites (single-atom catalyst) on the support [11]. The first two approaches aim to maximize the surface/volume (mass) ratio and to increase the number of surface-exposed Pt atoms. However, sophisticated preparations, low colorimetric signals, and the low number of sites for bioconjugation are the major drawbacks of these NPs. The elegant method for the efficient dispersion of Pt atoms on the surface of Au NPs was demonstrated by Gao et al.[10] The authors maintain the conditions (i.e., precursor injection rate) that provide a higher rate of the surface diffusion of Pt atoms than the rate of their deposition by the reduction. Thus, the Pt atoms spread across the Au surface and facilitate smooth Pt coverage with an adjustable thickness (1–10 layers). The applicability of the approach of precise control over deposition and diffusion rates was proven by the conformal coating of Pd NPs with Ru [12] and Ir [13], which demonstrated superior catalytic activities.

In this article, we propose the easy hydrothermal synthesis of trimetallic nanozyme with high PMA and low consumption of Pt precursor. The synthesis of trimetallic nanozymes includes three consistent steps. In the first step, Au NPs are synthesized by the reduction of $HAuCl_4$ with sodium citrate. In the next step, $AgNO_3$ is reduced by ascorbate in the presence of Au NPs, acting as the seeds with the formation of core@shell Au@Ag NPs.[14] In the third step, deposition of Pt is performed by the reaction of galvanic replacement: spontaneous electrochemical reactions driven by the difference of reduction potentials between Ag in Au@Ag NPs and $PtCl_6^{2-}$ in solution.[15] As a result of this process, the oxidation of Ag is accompanied by the reduction of ions from the solution and the Pt deposition on the NPs. The oxidation of the Ag atoms (as well as the reduction and deposition of Pt) is started on the surface [16,17] and then continued within a particle through the formation of pinholes, resulting in the formation of hollow nanoparticles [18].

The reactions occur on the solvent-exposed sites and, as we hypothesize, will facilitate the higher number of the surface-exposed Pt atoms in comparison with conventional spherical nanoparticles. Although the used approaches of the syntheses (i.e., overgrowth, galvanic replacement) are well-known, their usefulness for the synthesis of trimetallic NPs with high PMA and low consumption of Pt precursor was demonstrated for the first time. In the previous articles, nanozymes containing the same chemical composition but a different distribution of metals (core@shell@shell NPs and Au@Ag@Pt) were reported as the label in lateral flow immunoassay (LFIA) [19] and an enzyme-linked immunosorbent assay- (ELISA) like method [20]. Au@Ag@Pt NPs were synthesized by the consistent two-stage *in situ* reduction of Ag and Pt on seed NPs with the formation of Au@Ag and Au@Ag@Pt NPs. Although this approach results in the formation of unblocked Pt surface, layer-by-layer growth of Pt does not provide an optimal distribution of atoms and leads to the high consumption of Pt precursor. Thus, the proposed in this article approach of Pt distribution in Au@Ag–Pt NPs. and the use of these NPs as the label is novel.

To fully realize the potential of nanozymes as the optical and catalytic label, we used Au@Ag–Pt NPs as the label in LFIA. LFIA is based on the formation of immune complexes between antibodies and antigens during the migration of the liquid sample along the porous membrane with immobilized immunoreagents.[21] Nanozymes conjugated with antibodies act as the colorimetric label, and they facilitate the visual detection of immune complexes captured by antibodies immobilized in a membrane's test zone. If the target's concentration is low, then the minimal number of nanozymes is captured in the test zone, and a colorimetric signal is weak. A post-assay increase of the colorimetric signal is achieved by the accumulation of the product catalyzed by the nanozyme directly on the membrane.[22] Because LFIA is a routinely used point-of-care method, the low consumption of precious Pt precursors is especially in demand.

As the target analyte, we used C-reactive protein (CRP): the acute-phase inflammation biomarker widely controlled in routine clinical practice. The highly sensitive detection and the control of the dynamics of the CRP level in a broad range of concentrations are a necessary part of diagnostics and monitoring for therapy efficiency.[23]

## 2. Materials and methods

### 2.1. Materials

Native human CRP and two clones of monoclonal antibodies (mAb) against CRP (C2cc and C6cc clones) were purchased from HyTest (Moscow, Russia, www.hytest.fi). Goat antimouse antibodies were purchased from Arista Biologicals (Allentown, USA, www.aristabiologicals.com). Lyophilized human serum (TruLab N) was purchased from DiaSys (Holzheim, Germany, https://www.diasys-diagnostics.com/). Human serum and plasma were kindly provided by N. I. Pirogov City Clinical Hospital No. 1 (Moscow, Russia, http://gkb1.ru) and collected from volunteers and patients after

obtaining written and informed consent. Rabbit serum was obtained by centrifugation (10 min, 4,000 g) from blood after coagulation (5h at 37°C). Tetrachloroauric (III) acid, sodium hexachloroplatinate (IV), silver nitrate, nickel (II) sulfate hexahydrate, 3,3'-diaminobenzidine (DAB), 3,3',5,5'-tetramethylbenzidine (TMB), 30% hydrogen peroxide, sodium ascorbate, trisodium citrate, bovine serum albumin (BSA), streptavidin–peroxidase polymer, Au, Ag, and Pt standards for mass spectrometry were purchased from Sigma-Aldrich (St. Louis, USA, www.sigmaaldrich.com). All salts, acids, alkalis, and solvents were purchased from Chimmed (Moscow, Russia, www.chimmed.ru). ELISA was performed using polystyrene microplates 9018 provided by Corning Costar (Tewksbury, USA, www.corning.com). Lateral flow test strips were fabricated using nitrocellulose membranes CNPC-12, fiberglass conjugate release matrix PT-R5, and sample (GFB-R4) and absorbent (AP045) pads from Advanced Microdevices (Ambala Cantt, India, www. mdimembrane.com).

## 2.2. Apparatus

For the separation of nanoparticles, an Eppendorf centrifuge 5430 was used. The optical measurements were performed using the cuvette spectrophotometer Biochrom Libra S80 (Cambridge, UK, www.biochrom.co.uk) and the multifunctional plate reader PerkinElmer EnSpire Multimode Plate Reader (Waltham, USA, www.perkinelmer.com). The antibodies were dispensed on the membranes using an Imagene Technology IsoFlow dispenser (Hanover, USA). The guillotine cutter from A-Point Technologies Index Cutter-1 (Gibbstown, USA) was used to prepare the test strips. Digital images of the test strips after assay were obtained using a Canon 9000F Mark II scanner (Tokyo, Japan, www.canon.com). The size and the morphology of the NPs were studied by transmission electron microscopy using the Jeol JEM-1400 microscope (Tokyo, Japan, www.jeol.co.jp). Energy-dispersive spectroscopy (EDS) and EDS mapping were performed using

the transmission electron microscope Tecnai Osiris FEI equipped with the Super-X windowless EDX detector system (Hillsboro, USA, www.fei.com). The concentrations of Au, Ag, and Pt in the NPs were measured by inductively coupled plasma-mass spectrometry using the spectrometer Perkin-Elmer ELAN DRC-II (Waltham, USA, www.perkinelmer.com).

## 2.3. Synthesis of Au@Ag nanoparticles

Au NPs were synthesized by the reduction of tetrachloroauric acid with sodium citrate (the detailed procedure is described in the Supporting information). The aliquot of Au NPs (4 mL) was mixed with a sodium ascorbate solution (125 µL, 70 mM) and incubated for 30 s at room temperature with vigorous mixing. Then silver nitrate solution (375 µL) was added to the mixture using a peristaltic pump at the rate of 200 uL min$^{-1}$ until the final concentrations of silver nitrate were equal to 50 µM (Au@Ag #1 NPs), 100 µM (Au@Ag #2 NPs), 200 µM (Au@Ag #3 NPs), 500 µM (Au@Ag #4 NPs), 1,000 µM (Au@Ag #5 NPs), and 1,500 µM (Au@Ag #6 NPs). Reduction of the silver nitrate was performed at room temperature for 20 min. Synthesized Au@Ag NPs were stored in the dark at room temperature.

## 2.4. Synthesis of Au@Ag–Pt nanoparticles

Au@Ag NPs were separated from the excess of the ascorbic acid by centrifugation (15,000 g, 15 min) and redispersed in an equal volume of water. Considering that single-Pt atom deposition leads to the replacement of four Ag atoms, the final concentrations of $Na_2PtCl_6$ varied with a range from 8 to 0.12 for the ratio ($Pt^{4+}/Ag^+$). Detailed protocols are described in the Supporting information and summarized in Table S1.

## 2.5. Conjugation of nanoparticles with antibodies

The conjugation of all three types of NPs (Au, Au@Ag, Au@Ag–Pt NPs) with antibodies was performed following the same procedure. The pH value of NP suspension was adjusted to 8.5 with a

0.2M $K_2CO_3$ solution. The concentrations of antibodies for the conjugation were determined using flocculation curves (the detailed procedure is described in the Supporting information). The mAb to CRP (C6cc clone) were mixed with the suspension of NPs (12 µg mL$^{-1}$ for Au NPs, 11 µg mL$^{-1}$ for Au@Ag NPs, and 10 µg mL$^{-1}$ for Au@Ag–Pt NPs) and incubated for 90 min with slight agitation. BSA was added to its final concentration of 0.15%, and NPs were separated by centrifugation (20,000 g for 25 min for Au NPs; 16,000 g for 20 min for Au@Ag and Au@Ag–Pt NPs). Conjugates were redispersed in 20 mM of Tris buffer pH 7.5 containing 0.25% BSA, 0.25% Tween-20, and 1% sucrose and stored at 4°C.

## 2.6. Test strip preparation

Antimouse IgG (1 mg mL$^{-1}$) and mAb to CRP (C2cc clone, 1 mg mL$^{-1}$) in 50 mM of potassium phosphate buffer with 0.05 M of NaCl, pH 7.4 (PBS), were dispended (0.15 µL mm$^{-1}$) at the control and test zones (CZ and TZ, respectively) on the nitrocellulose membrane CNPC-12. Fiberglass membrane PT-R5 was soaked (1.5 µL mm$^{-1}$) with NPs conjugates (OD$_{\lambda max}$ = 4.0). All membranes were dried at 30°C for 24 h; then, the sample and the absorbent pads were glued. After cutting, the test strips were stored in zip pockets at room temperature.

## 2.7. Lateral flow immunoassay

Four formats of LFIA were performed using different NPs as the label: that is, Au NPs (LFIA-1), Au@Ag NPs (LFIA-2), Au@Ag–Pt NPs acting as the colorimetric label (LFIA-3), and Au@Ag–Pt NPs acting as the label with PMA (LFIA-4). All four formats were performed following the same procedure. For calibration plots, rabbit serum was diluted 4 times with PBST and spiked with CRP (1,000–0.004 ng mL$^{-1}$). For the analysis of real samples, human plasma and serum were diluted (4–200 times) with PBST. The test strips were immersed vertically in the sample (100 µL) and incubated for 5 min. For LFIA-4, a substrate solution (0.05% DAB, 200 mM $H_2O_2$, 0.05%

NiSO$_4$*7H$_2$O in 50 mM PBS, pH 7.3) was dropped (10 µL) on the test strips after completion of LFIA-3 and incubated for 5 min. The test strips were scanned, and the values of the intensity of coloration of the TZs in the gray-scale mode were calculated using TotalLab TL120 software (Nonlinear Dynamics, UK, www.totallab.com). For the calibration plots, each concentration was studied in triplicate. The real samples were studied in duplicate. The limit of detection (LOD) values were determined as the concentration providing a colorimetric signal higher than the sum of the colorimetric signal of the blank probe and its 3 standard deviations.

## 3. Results and discussion

## 3.1. Characterization of Au and Au@Ag nanoparticles

The Au NPs were synthesized using the citrate reduction method. The mean diameter of Au NPs was equal to 17.9 ± 1.4 nm, and no aggregates were observed (Figure 1a, Figure S1 a,b). The shape of Au NPs was close to spherical, and the elongation coefficient (ratio of major axis length of the particle to the minor axis length, Table S2) was equal to 1.07 ± 0.07. The results confirm the homogeneity and colloidal stability of Au NPs and their applicability as the seeds for the formation of the silver shell.

The reduction of silver nitrate in the suspension of Au NPs leads to the formation of core@shell Au@Ag NPs (Figure 1 b-c, Figure S1 c-n). The mean diameters and elongation coefficients of Au@Ag NPs are summarized in Table S2. The formation of the silver layer around Au NPs results in the shift of $\lambda_{max}$ and the increase of the absorbance value (Figure 1d).
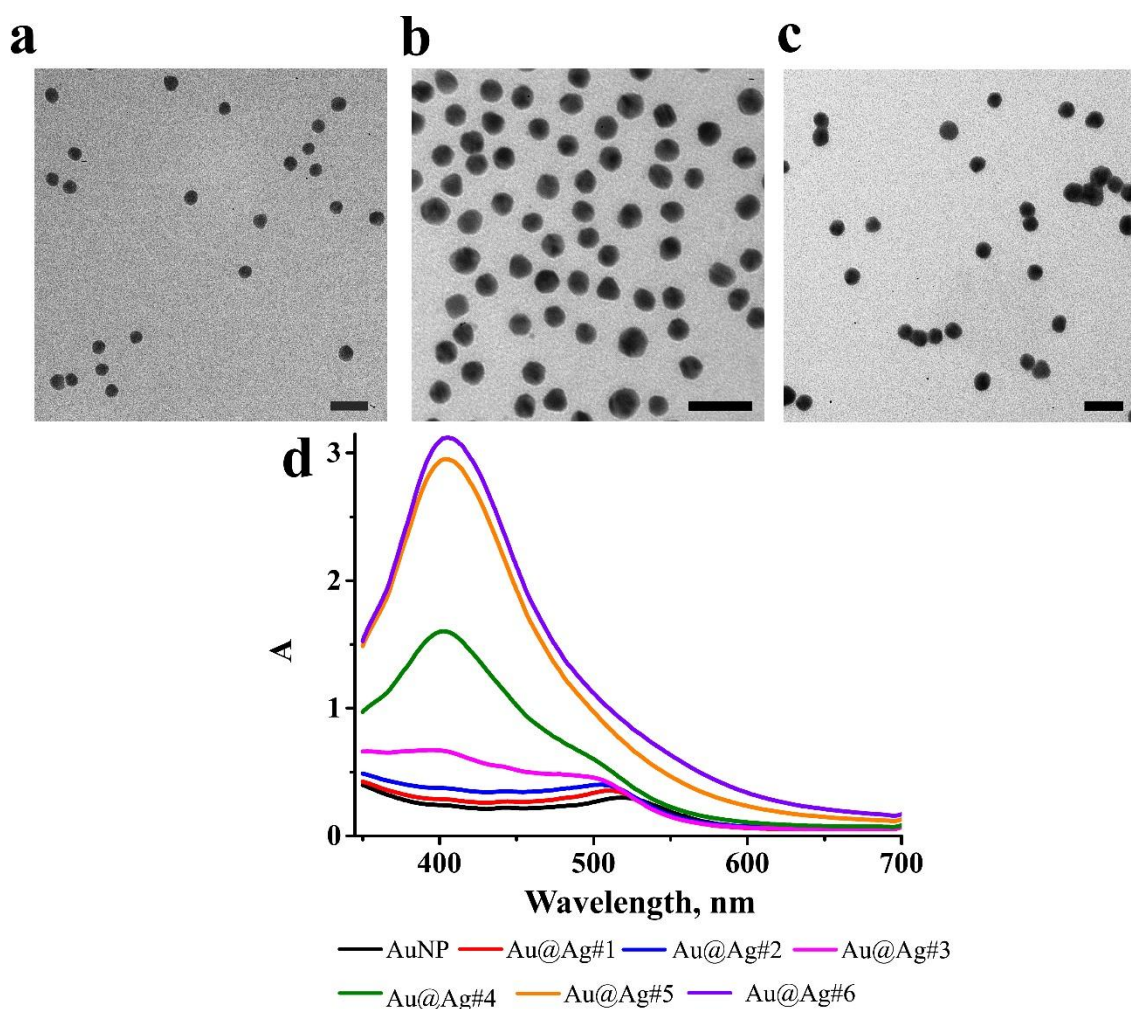
**Figure 1.** Characteristics of Au and Au@Ag NPs. TEM microphotographs of Au NPs (a), Au@Ag #2 (b), and Au@Ag #3 (c). The scale bar is equal to 50 nm. Absorbance spectra of Au and Au@Ag #1–6 NPs (d). All NPs were used as synthesized, without dilutions.

The results of EDS confirm the presence of Ag in the synthesized NPs (Figure S2). Au@Ag NPs synthesized with the concentration of silver nitrate $\geq$ 500 µM (Au@Ag #4–6) result in the formation of polydispersed NPs (histograms of the diameter distribution of NPs and TEM microphotographs are presented in Figure S1 c-n) with nonuniform silver coatings.

The formation of the silver layer was proven by the increase of the hydrodynamic size of NPs (Figure S3) and EDS mapping of Au@Ag #2 NPs (Figure 2) and Au@Ag #4 NPs (Figure S4, 5). Ag atoms are spread over the whole surface of Au NPs (Figure 2b) and form the shell (Figure 2c). The relative contents of Au and Ag are dependent on the concentrations of precursors and were equal to 60.2 and 39.8% for Au@Ag #4 NPs and 73.2 and 26.7% for Au@Ag #2 NPs, respectively.
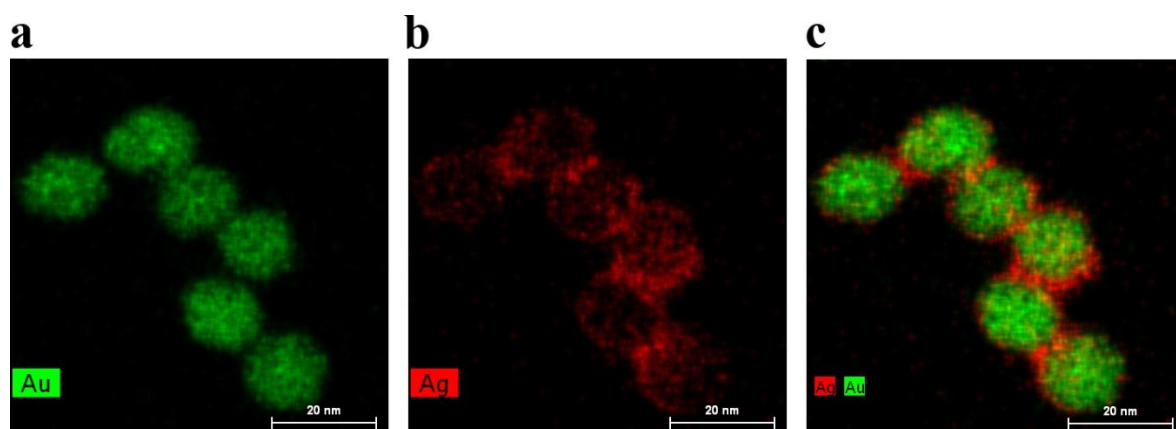


**Figure 2.** The distribution of elements in Au@Ag #2 NPs obtained by EDS mapping: for Au (**a**), for Ag (**b**), and for combined distribution of Au and Ag (**c**).

For the deposition of platinum, galvanic replacement was performed for Au@Ag #1, 3, 5, and 6 NPs with an equal ratio of $Pt^{4+}$/Ag concentrations (Table S1). For Au@Ag #2 and #4 NPs, the influence of different ratios of $Pt^{4+}$/Ag on the size, optical properties, and morphology of NPs was studied in a broad concentrations ration ($Pt^{4+}$/Ag within 8–0.07 for Au@Ag #2 NPs and 4–0.005 for Au@Ag #4 NPs, Table S1).

The changes of the concentrations of Pt during the galvanic replacement in Au@Ag #2–Pt #1–7 NPs were monitored with ICP-MS (Figure 3 a, b).

11
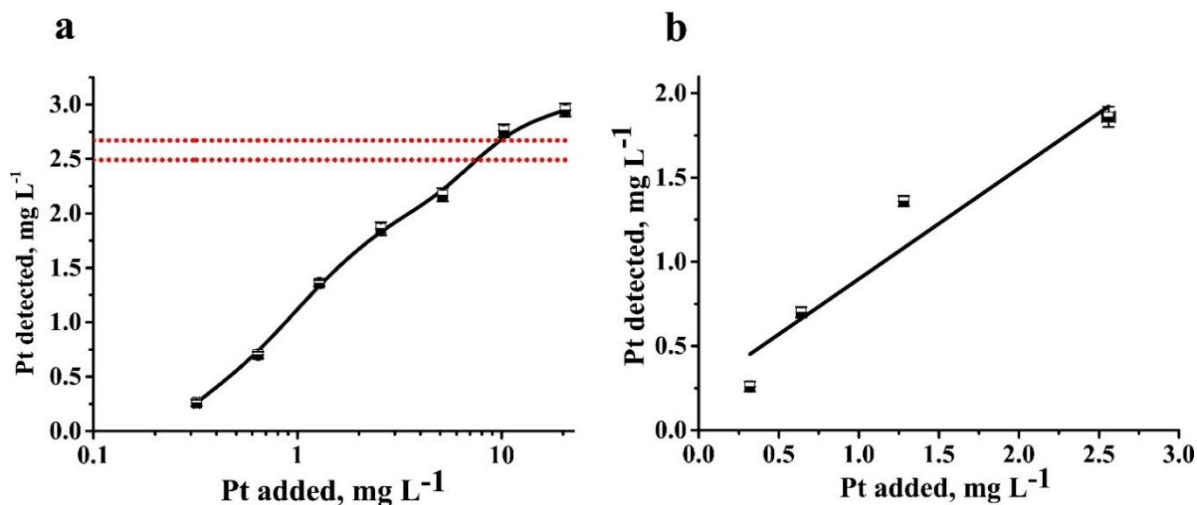
**Figure 3.** Measurement of the Pt in Au@Ag #2–Pt NPs by ICP-MS. The dependence of the Pt detected in Au@Ag #2–Pt NPs from the added concentrations of Pt. The area between 2 red-dotted lines corresponds to the maximum predicted concentration of Pt (**a**). The dependence of the Pt detected in Au@Ag #2–Pt NPs from the added concentrations of Pt at the concentrations below the maximum predicted concentrations of Pt. $R^2 = 0.909$ (**b**).

The concentrations of Pt in Au@Ag #2–Pt NPs are dependent on the added amount of $PtCl_6^{2-}$ ions only in the area where the ratio of $Pt^{4+}/Ag \leq 1$. Although the added concentrations of Pt for Au@Ag #2–Pt #1–3 were high (20.5 ± 0.3, 10.25 ± 0.17, and 5.13 ± 0.08 mg $L^{-1}$), the detected concentrations of Pt in Au@Ag #2–Pt #1–3 NPs were significantly lower (2.95 ± 0.06, 2.76 ± 0.06, and 2.17 ± 0.06 mg $L^{-1}$ of Pt, Figure 3a). This fact confirms the deposition of Pt is performed by galvanic replacement and is thus limited by the concentration of Ag in the Au@Ag #2 NPs. According to ICP-MS measurements, the concentration of Ag in Au@Ag #2 NPs was equal to 5.7 ± 0.2 mg $L^{-1}$, limiting the maximum predicted amount of deposited platinum to 2.49–2.67 mg $L^{-1}$ (Figure 3a, the area between red-dotted lines). The excess of the added $PtCl_6^{2-}$ ions is not deposited on the particles because of the absence of the reducing agents. By contrast, the concentrations of Pt

in Au@Ag #2–Pt #4–7 NPs (i.e., equal and below the value of the maximum predicted amount of deposited platinum, i.e., $Pt^{4+}/Ag \leq 1$) demonstrated a good correlation with the added concentrations of platinum (Figure 3b). This proves the deposition of platinum in nanoparticles was achieved by galvanic replacement.

   Galvanic replacement results in the change of the NPs' morphology because the replacement of four Ag leads to the addition of the single Pt atoms: $3Ag^0 + PtCl_6^{2-} \rightarrow 3Ag^+ + Pt^0 + 6\ Cl^-$. As the galvanic replacement continues, the inequivalent replacement leads to the formation of pinholes, voids, and finally hollow particles. Au@Ag #1–3 NPs have a thin Ag shell, and the galvanic replacement of Ag atoms does not lead to the change of the morphology of NPs (Figure 4a, Figure S6 a–j). The formation of voids after galvanic replacement was observed for only Au@Ag #4–6 NPs (i.e., for NPs with a thick enough Ag shell; Figure 4 b, c, Figure S 6 k–p). The diameter of the intrinsic particles is equal to the initial GNP, and the size of the voids corresponds to the thickness of the silver layers. Galvanic replacement results in the shift of maximum absorbance wavelength to the long-wave region (Figure 4d). Thus, the formation of Au@Ag–Pt NPs during galvanic replacement provides precise control over not only composition and uniform spreading of Pt atoms but also morphology invariant (using Au@Ag #1–3 as the templates) and variant (using Au@Ag #4–6 as the templates) approaches for the manipulation of the optical properties (Figure 4D, Figure S6), which can be further used for highly sensitive and multiplex bioanalysis. [24,25]
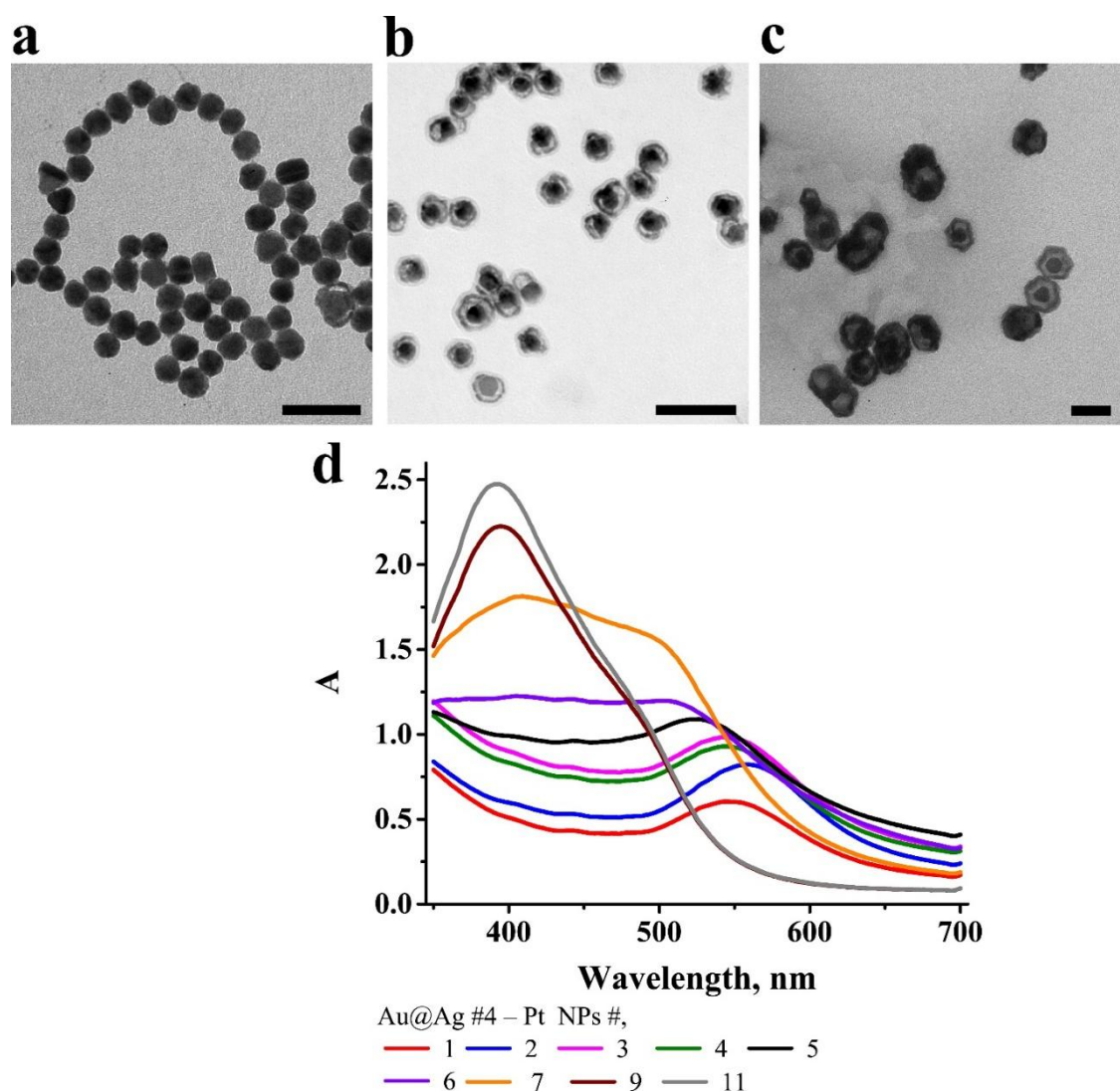
**Figure 4.** Characteristics of NPs synthesized by galvanic replacement, Au@Ag #2–Pt #4 NPs (**a**), Au@Ag #4–Pt #4 NPs (**b**), and Au@Ag #6–Pt NPs (**c**); The scale bar is equal to 50 nm. Absorbance spectra of Au@Ag #4 and NPs obtained by galvanic replacement (**d**).

EDS was used for the study of the distribution of metals in NPs (Figure 5). The results of the mapping show uniform distribution of Pt atoms across NPs (Figure 5a). Au atoms do not participate in the galvanic replacement reaction and remain concentrated in the core area of NPs (Figure 5b). The results of EDS demonstrate the presence of all three metals in Au@Ag #2–Pt #4 NPs. Chemical

mapping of NPs confirms the uniform distribution (both in Ag shell areas and in the middle of NPs) of Pt atoms (Figure S7). Because of the low concentration of Pt and its uniform distribution in the NPs, its characteristics' peaks have low intensity (Figure 5c). The relative contents of Au, Ag, and Pt were equal to 63.7, 23.0, and 13.3%.
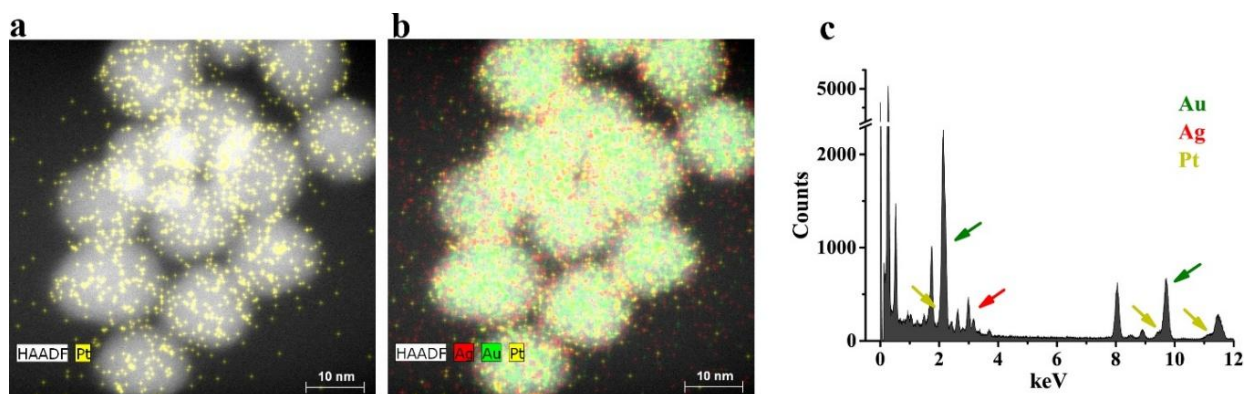


**Figure 5.** Distribution of elements in Au@Ag #2−Pt #4 NPs obtained by EDS mapping: for Pt (**a**), for Au, Ag, and Pt (**b**). EDX spectra of NPs: Peaks of elements are shown with colored arrows; Lα and Lβ lines were registered (**c**).

For further developments, we focused on the Au@Ag #2 NPs and on the NPs obtained by galvanic replacement from them. The choice was determined by the relatively low Ag concentration, which facilitates the formation of Au@Ag–Pt NPs with the low load of Pt. The low consumption of the precious Pt precursor for the production of nanozymes with high PMA is highly desirable for practical use.

In the proposed method, the deposition of platinum achieved by galvanic replacement facilitates the formation of the dispersed catalytic sites on the surface of NPs. The conventional methods of Pt coating by the reduction of precursors result in Volmer–Weber growth (i.e., growth of Pt islands on the surface rather than covering) on Au and Ag substrates [26,27], which are not efficient for catalysis

because of the high fraction of the buried platinum atoms.[28] Compared with layer-by-layer growth, where precise control over diffusion and deposition rates is required, the developed approach's driving force (difference in standard reduction potentials) provides an easy, rapid, and reproducible synthesis procedure.

## 3.2. Peroxidase-mimicking activity of nanoparticles

PMA was monitored by oxidation of TMB with $H_2O_2$ in the presence of Au@Ag #2–Pt #4 NPs (Figure 6 a, b). Specific activity (SA) was calculated to mg of Au because Au NPs do not participate in the galvanic replacement reaction, and the deposition of Ag and Pt occurs on only Au NPs. Neither Au NP nor Au@Ag #1–6 NPs demonstrated PMA.
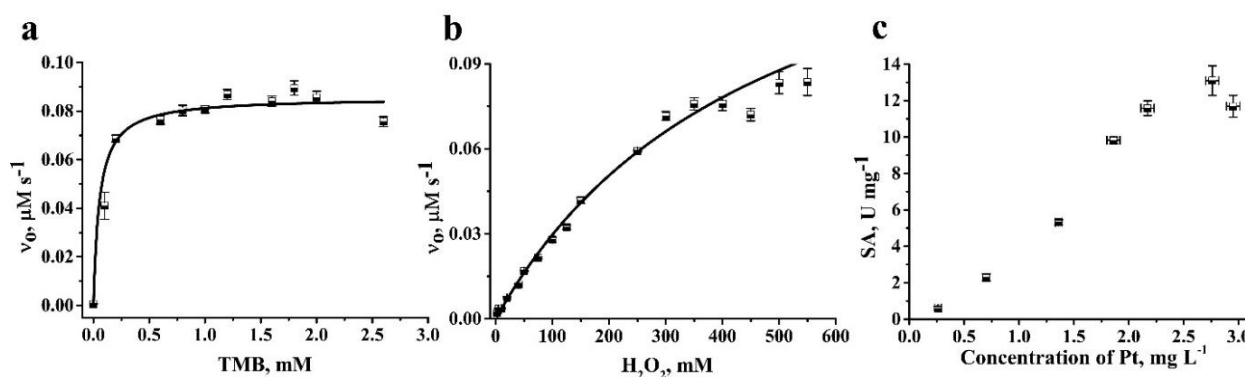


**Figure 6.** Characteristics of the PMA of Au@Ag #2–Pt #4 NPs. The effects of the concentrations of substrates on the initial velocities of TMB oxidation. For TMB (concentration of $H_2O_2$ is equal to 1M) (**a**). For $H_2O_2$ (concentration of TMB is equal to 0.2 mM) (**b**). The relationship between SA and the concentration of Pt in Au@Ag #2 Pt #1–7 NPs (**c**).

Km values measured for both substrates were equal to 0.06 mM for TMB and 320 mM for $H_2O_2$. However, as shown in the review by Wu et al. [29], the reported values of kinetic constants for various

Pt-containing nanozymes are varied in a broad range (up to 2–3 folds). Thus, for the precise comparison of the PMA of nanozymes, the SA values can be used.[30] The SA values for Au@Ag #2–Pt #1–7 NPs were calculated (SA values are summarized in Table S3). NPs synthesized in excess of Pt over the predicted load (i.e., $Pt^{4+/}Ag > 1$) demonstrated comparable SA values (Figure 6c, Table S3). This observation also proves the deposition of Pt is performed only by the galvanic replacement of Ag in NPs. Hence, Au@Ag #2–Pt #1–3 NPs are synthesized in the high concentration of Pt precursor; their SA is determined by the deposited in NPs concentration of Pt, which is related to the concentration of Ag. Thus, the SA values of Au@Ag–Pt NPs can be regulated by changing the Ag precursor concentration during the synthesis of Au@Ag NPs and by the Pt precursor concentration during galvanic replacement.

Comparison of the SA values for Au@Ag–Pt with the previously published SA values for nanozymes demonstrates higher SA values of synthesized Au@Ag–Pt nanozymes achieved with lower consumption of the Pt precursor. The SA value of Au@Ag–Pt NPs was about 20 times higher than for Au@Pt nanoparticles synthesized by the reduction of $Na_2PtCl_6$ on Au NPs.[31]

The SA value of Au@Ag #2–Pt #4 NPs was about 80% compared to Au@Ag #2–Pt #1–4 NPs. However, the synthesis of Au@Ag #2–Pt #4 NPs required 2–8 times lower consumption of Pt precursor in comparison with Au@Ag #2–Pt #1–3 NPs. Considering the balance of Pt precursor consumption and PMA, we selected Au@Ag #2–Pt #4 NPs for further use as the label for LFIA.

## 3.3. Conjugation of nanoparticles with antibodies, optimization of lateral flow immunoassay

Conjugation of mAb with NPs was performed by physical adsorption which ensures the synthesis of highly-stable conjugates and retains antigen-binding properties of adsorbed mAb.[32] The concentrations of mAb for the conjugation with NPs were selected using the flocculation curves

method, which determines the stability of conjugates in the solution with high ionic strength. Coating NPs with mAb prevents particles' aggregation controlled by NPs' absorbance spectrum (Figure S8). For the conjugation with NPs, the concentrations of mAb exceeding the minimal stabilized concentration (concentrations of mAb at which the curve reaches the plateau) at 30% were used (Figure S9). These included 12, 11, and 10 µg mL$^{-1}$ for Au NPs, Au@Ag NPs, and Au@Ag #2–Pt #4 NPs, respectively. The lower concentration of mAb was used for the conjugation with Au@Ag #2–Pt #4 NPs to avoid dense coverage of the surface of NPs that may cause the reduction of PMA.[33]

Adsorption of mAb on the surface of NPs results in the increase of hydrodynamic diameters from 23.5 ± 5.6 nm to 50.1 ± 13.1 nm for Au NPs and their conjugate with mAb (Figure S10 a), from 27.4 ± 8.8 nm to 69.0 ± 24.4 nm for Au@Ag #2 NPs and their conjugate with mAb (Figure S10 b) and from 36.3 ± 9.0 nm to 80.7 ± 36.6 nm for Au@Ag #2–Pt #4 NPs and their conjugate with mAb (Figure S10 c).

The concentration of mAb conjugated to Au@Ag #2–Pt #4 NPs was determined by ELISA (Figure S11) as the difference between the concentrations of added and detected biotinylated mAb in the supernatant after conjugation. The results show all three types of NPs bound about 80% of added mAb. Synthesized conjugates were stable, and no aggregates were observed (Figure S10). The conditions that provide the highest colorimetric signal (C2cc clone immobilized in TZ, C6cc clone conjugated to NPs, Figure S 12) were used in all further experiments.

## 3.4. Application of nanoparticles as the colorimetric and catalytic labels in lateral flow immunoassay

NPs act as the labels in LFIA, providing visual detection of immunocomplexes in TZ and CZ (Figure 7 a–c). Conjugates of mAb with NPs were used as the colorimetric (LFIA-1–3) and catalytic

label (LFIA-4). Au NPs were used as the conventional label in LFIA. Au@Ag #2–Pt #4 NPs were selected as the catalytic label based on the balance between low consumption of Pt precursor during synthesis and relatively high PMA. The comparison of LOD values between LFIA-1–3 will facilitate the estimation of the impact of the NPs' optical properties. The comparison of LOD values between LFIA-3 and LFIA-4 will facilitate the estimation of the impact of the catalytic properties of Au@Ag #2–Pt #4 NPs.
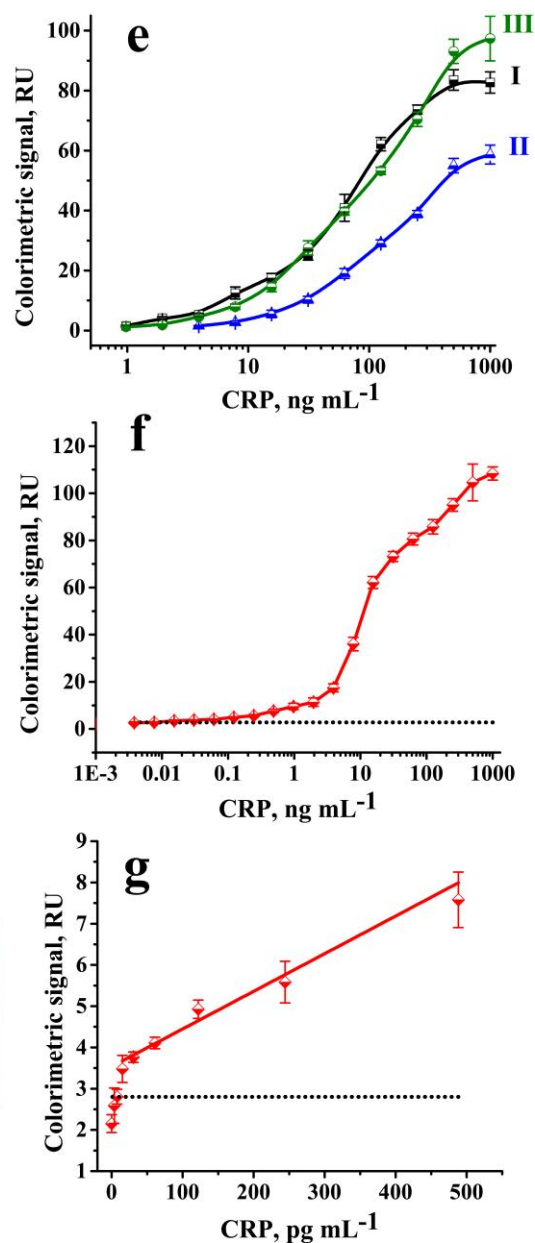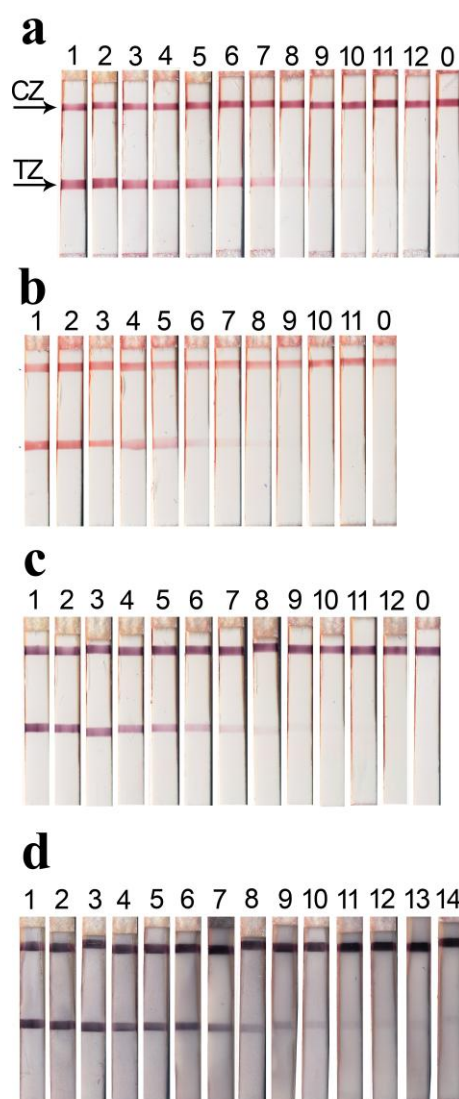
**Figure 7.** LFIA of CRP in serum using different NPs as the labels. The test strips after LFIA-1 (**a**), LFIA-2 (**b**), LFIA-3 (**c**), and LFIA-4 (**d**). The numbers above the test strips correspond to the concentration of CRP, ng mL$^{-1}$: 1 – 1,000, 2 – 500, 3 – 250, 4 – 125, 5 – 62.5, 6 – 31.2, 7 – 15.6, 8 – 7.8, 9 – 3.9, 10 – 1.9, 11 – 0.98, 12 – 0.49, 13 – 0.244, and 14 – 0.122; concentration of CRP, pg mL$^{-1}$, 15 – 61, 16 – 30, 17 – 15, and 18 – 7; and 0 – blank probe. Calibration curves for: LFIA-1 (I), LFIA-2 (II), and LFIA-3 (III) (**e**), LFIA-4 (**f**), plot at low CRP concentrations. The black-dotted line corresponds to the background (**g**).

The LOD values were equal to 3.9 ng mL$^{-1}$ for LFIA-2 (Figure 7e, plot II), 980 pg mL$^{-1}$ for LFIA-1 and LFIA-3 (Figure 7e, plots I and III), and 15 pg mL$^{-1}$ for LFIA-4 (Figure 7 f, g).

The higher LOD value for LFIA-2 could be explained by the similar coloration of Au@Ag NPs with serum. Thus, visual and instrumental detection is hindered by staining the membrane with the sample (Figure 7 b). Red- and violet-colored Au and Au@Ag–Pt NPs (Figure 7 a, c) form contrasting TZs and CZs and could be detected simply visually and instrumentally. Because of the similar optical properties of Au and Au@Ag–Pt NPs, the decrease of LOD values was not achieved, and the colorimetric signal of TZs demonstrated the comparable values (Figure 7 e, plots I and III).

The use of PMA of Au@Ag–Pt NPs facilitates the significant increase of the colorimetric signals in TZs and CZs achieved by the accumulation of the dark-colored insoluble product of DAB oxidation. An optimization study showed a five-minute incubation of the substrate on the test strip provides high amplification of the colorimetric signal and the absence of nonspecific staining (Figure S13). The LOD value of LFIA-4 was about 65 times lower in comparison with LFIA 1 and 3. Previously published articles describing the use of Pt-containing nanozymes report the decrease

of LOD values in the range of 10 to 2,000 times (Table S4). However, the concentrations of Pt precursors were significantly higher (Table S4).

Compared with other LFIA for CRP, LFIA-4 provides the lowest LOD value among equipment-free LFIA (Table S5). The LOD value is comparable with the values reported for electrochemical assays (i.e., 5.9 pg mL$^{-1}$ and 15 pg mL$^{-1}$). [34,35] However, the reported electrochemical methods are more time consuming (40–50 min).

The drawback of the LFIA-4 is the necessity of the additional substrate addition stage, which increases the assay time. Despite this additional stage, LFIA-4 preserves the benefits of the rapid point-of-care method (total assay time within 10 min).


## 3.5. Validation of lateral flow immunoassay on real samples

LFIA-3 and LFIA-4 were validated on real samples of human plasma, serum, and capillary blood. The accuracy of LFIA-3 and LFIA-4 was evaluated by the recovery studies of spiked rabbit serum (Figure S14) and the correlation of the quantitative results with ELISA in diluted human plasma (Figure S15). Recovery studies demonstrated a recovery range of 86.6–117.0% for LFIA-3 (correlation coefficient between added and measured CRP is equal to $R^2 = 0.967$) and of 83.7–116.2% for LFIA-4 (correlation coefficient between added and measured CRP is equal to $R^2 = 0.987$). The quantitative results of LFIA-3 and LFIA-4 demonstrated high correlation with ELISA ($R^2 = 0.99$ for LFIA-3, and $R^2 = 0.986$ for LFIA-4). No false-positive and false-negative results were observed.

Because of the assay's high sensitivity, a small amount of the sample may be collected and diluted by buffer solutions to the volumes required for the assay (70–100 µL). Considering the significant increase of CRP levels during infections and sepsis [36] and the high sensitivity of LFIA-4, the ultra-

low volume of the sample is required ($\approx 0.2$ μL of biological sample diluted to 100 μL of buffer). This provides the possibility of performing LFIA-4 using capillary blood. The collection of the capillary blood is an easy and less traumatic procedure (compared to vein blood collection), which can be done in the point-of-care testing by a user without medical training (i.e., using a conventional lancet pen device).

The preliminary results demonstrated the applicability of LFIA-4 for the detection of CRP in capillary blood (Figure S16). For capillary blood samples 5–7, the colorimetric signal of TZ for LFIA-3 and LFIA-4 demonstrated close values that can be explained by the high background staining of the test strips and therefore the lower value of the signal-to-noise ratio. The growth of the background is explained by the presence of nonenzymatic compounds with PMA (i.e., hemoglobin, which arises from the hemolysis of erythrocytes during blood collection, as well as other Fe-containing proteins).[37] The elimination of the background will require the further optimization of the assay parameters. For capillary blood samples 1, 2, 3, and 8, LFIA-4 demonstrated a significant increase of the colorimetric signal (up to 12 times) in comparison with LFIA-1 and facilitated the conventional visual detection of the more contrasted TZs. Samples 4 and 9 demonstrated false-negative results obtained by LFIA-1 and LFIA-3, whereas LFIA-4 showed visually and instrumentally distinguished coloration of TZ (Figure S16).

## 4. Conclusion

Trimetallic nanozyme consisting of Au core, Ag shell, and the surface-exposed Pt atoms (Au@Ag–Pt) were synthesized. Uniform distribution of Pt on the surface of the nanozyme facilitates high metal utilization and boosts the particles' peroxidase-mimicking activity. In comparison with

previously synthesized core@shell Au@Pt nanoparticles, Au@Ag–Pt demonstrated 20 times higher peroxidase-mimicking activity.

The use of Au@Ag–Pt nanoparticles as the catalytic label provides a 65 times lower limit of detection of lateral flow immunoassay of C-reactive protein in serum in comparison with conventional assay with Au nanoparticles. The limit of the detection of C-reactive protein was reduced to 15 pg mL$^{-1}$: the lowest among equipment-free lateral flow immunoassays. Because of its high sensitivity, the assay requires a small amount of the sample (0.2 µL) and may be used for self-testing by unskilled persons.

ASSOCIATED CONTENT

**Supporting Information**

The following files are available free of charge.

Figures (Figures S1–S16)

TEM microphotographs of Au and Au@Ag #1–6 NPs; EDX spectra of Au@Ag #2 NPs; Distribution of hydrodynamic diameters of Au, Au@Ag #2, and Au@Ag #4 NPs; HAADF microphotograph and EDS-TEM mapping of Au and Ag in Au@Ag #2 NPs; Distribution of Au and Ag in Au@Ag #4 NPs; TEM microphotographs of Au@Ag–Pt NPs; Distribution of Au, Ag, and Pt in Au@Ag #4 NPs; Absorbance spectra of Au, Au@Ag #2, and Au@Af #2–Pt #4 NPs with the different amount of mAb after addition of NaCl; Flocculation curves for Au, Au@Ag #2, and Au@Af #2–Pt #4 NPs; Distribution of hydrodynamic diameters of conjugates of Au, Au@Ag #2, and Au@Ag #4 NPs with mAb; Calibration plots for the measurement of biotinylated mAb concentration; Optimization of LFIA with two clones of mAb; Effect of the substrate incubation

time on the colorimetric signal of TZ; Correlation between added and detected concentrations of CRP in rabbit serum; Correlation between concentration of CRP measured by ELISA and LFIA in human plasma; LFIA of CRP in capillary blood.

Tables (Tables S1–S5)

Composition of Au@Ag–Pt NPs; Sizes and elongation coefficients of Au and Au@Ag NPs; SA values for Au@Ag #2–Pt #1–7 NPs; Comparison of LOD reducing and Pt consumption with previously published results; Comparison of LOD values of LFIA of CRP.

## AUTHOR INFORMATION

**Boris B. Dzantiev** (corresponding author): A.N. Bach Institute of Biochemistry, Federal Research Centre "Fundamentals of Biotechnology" of the Russian Academy of Sciences, Leninsky prospect 33, 119071 Moscow, Russia; email: dzantiev@inbi.ras.ru.

**Author Contributions**

The manuscript was written through the contributions of all authors. All authors have given approval to the final version of the manuscript.

**Notes**

The authors declare no competing financial interests. Blood samples from patients and volunteers were collected after obtaining written and informed consent. Any patients' personal data are not disclosed.

The data (optical spectra, EDS spectra, kinetics data, calibration plots for LFIA and ELISA, validation of LFIA) that support the findings of this study are available on www.chemrxiv.org

## References

(1) Jin, S.; Wu, C.; Ye, Z.; Ying, Y. Designed inorganic nanomaterials for intrinsic peroxidase mimics: a review. *Sensors Actuators B Chem.* **2019**, *283*, 18–34. https://doi.org/10.1016/j.snb.2018.10.040.

(2) Yang, H.; He, Q.; Chen, Y.; Shen, D.; Xiao, H.; Eremin, S. A.; Cui, X.; Zhao, S. Platinum nanoflowers with peroxidase-like property in a dual immunoassay for dehydroepiandrosterone. *Microchim. Acta* **2020**, *187* (11), # 592 https://doi.org/10.1007/s00604-020-04528-9.

(3) Panferov, V. G.; Safenkova, I. V.; Zherdev, A. V.; Dzantiev, B. B. The steadfast Au@Pt Soldier: peroxide-tolerant nanozyme for signal enhancement in lateral flow immunoassay of peroxidase-containing samples. *Talanta* **2021**, *225*, # 121961. https://doi.org/10.1016/j.talanta.2020.121961.

(4) Wei, Z.; Xi, Z.; Vlasov, S.; Ayala, J.; Xia, X. Nanocrystals of platinum-group metals as peroxidase mimics for: in vitro diagnostics. *Chem. Commun.* **2020**, *56* (95), 14962–14975. https://doi.org/10.1039/d0cc06575g.

(5) Lori, O.; Elbaz, L. Recent advances in synthesis and utilization of ultra-low loading of precious metal-based catalysts for fuel cells. *ChemCatChem* **2020**, *12* (13), 3434–3446. https://doi.org/10.1002/cctc.202000001.

(6) Rodrigues, T. S.; Da Silva, A. G. M.; Camargo, P. H. C. Nanocatalysis by noble metal nanoparticles: controlled synthesis for the optimization and understanding of activities. *J. Mater. Chem. A* **2019**, *7* (11), 5857–5874. https://doi.org/10.1039/c9ta00074g.

(7)   G., N.; Casals, E.; Ojea, I.; Varon, M.; Puntes, V. The reactivity of colloidal inorganic nanoparticles. In Book *The Deliery of Nanoparticles,*InTech Open, **2012**, 377–400. https://doi.org/10.5772/35238.

(8)   Meng, X.; Zare, I.; Yan, X.; Fan, K. Protein-protected metal nanoclusters: an emerging ultra-small nanozyme. *WIREs. Nanomedicine Nanobiotechnology* **2020**, *12* (3), e1602. https://doi.org/10.1002/wnan.1602.

(9)   Yang, T.; Ahn, J.; Shi, S.; Wang, P.; Gao, R.; Qin, D. Noble-metal nanoframes and their catalytic applications. *Chem. Rev*. **2021**, *121* (2), 796–833. https://doi.org/10.1021/acs.chemrev.0c00940.

(10)  Gao, Z.; Ye, H.; Tang, D.; Tao, J.; Habibi, S.; Minerick, A.; Tang, D.; Xia, X. Platinum-decorated gold nanoparticles with dual functionalities for ultrasensitive colorimetric in vitro diagnostics. *Nano Lett.* **2017**, *17* (9), 5572–5579. https://doi.org/10.1021/acs.nanolett.7b02385.

(11)  Jiao, L.; Xu, W.; Wu, Y.; Yan, H.; Gu, W.; Du, D.; Lin, Y.; Zhu, C. Single-atom catalysts boost signal amplification for biosensing. *Chem. Soc. Rev.* **2021**, *50*, 750-765. https://doi.org/10.1039/D0CS00367K.

(12)  Ye, H.; Wang, Q.; Catalano, M.; Lu, N.; Vermeylen, J.; Kim, M. J.; Liu, Y.; Sun, Y.; Xia, X. Ru nanoframes with an fcc structure and enhanced catalytic properties. *Nano Lett.* **2016**, *16* (4), 2812–2817. https://doi.org/10.1021/acs.nanolett.6b00607.

(13)  Xia, X.; Figueroa-Cosme, L.; Tao, J.; Peng, H. C.; Niu, G.; Zhu, Y.; Xia, Y. facile synthesis of iridium nanocrystals with well-controlled facets using seed-mediated growth. *J. Am. Chem. Soc.* **2014**, *136* (31), 10878–10881. https://doi.org/10.1021/ja505716v.

(14) Bai, T.; Wang, M.; Cao, M.; Zhang, J.; Zhang, K.; Zhou, P.; Liu, Z.; Liu, Y.; Guo, Z.; Lu, X. Functionalized Au@Ag-Au Nanoparticles as an optical and SERS dual probe for lateral flow sensing. *Anal. Bioanal. Chem.* **2018**, *410* (9), 2291–2303. https://doi.org/10.1007/s00216-018-0850-z.

(15) Da Silva, A. G. M.; Rodrigues, T. S.; Haigh, S. J.; Camargo, P. H. C. Galvanic replacement reaction: recent developments for engineering metal nanostructures towards catalytic applications. *Chem. Commun.* **2017**, *53* (53), 7135–7148. https://doi.org/10.1039/c7cc02352a.

(16) Russo, L.; Merkoçi, F.; Patarroyo, J.; Piella, J.; Merkoçi, A.; Bastús, N. G.; Puntes, V. Time- and size-resolved plasmonic evolution with nm resolution of galvanic replacement reaction in AuAg nanoshells synthesis. *Chem. Mater.* **2018**, *30* (15), 5098–5107. https://doi.org/10.1021/acs.chemmater.8b01488.

(17) Londono-Calderon, A.; Bahena, D.; Yacaman, M. J. Controlled synthesis of Au@AgAu Yolk-Shell cuboctahedra with well-defined facets. *Langmuir* **2016**, *32* (30), 7572–7581. https://doi.org/10.1021/acs.langmuir.6b01888.

(18) Liu, X.; Astruc, D. From Galvanic to anti-galvanic synthesis of bimetallic nanoparticles and applications in catalysis, sensing, and materials science. *Adv. Mater.* **2017**, *29* (16), # 1605305 https://doi.org/10.1002/adma.201605305.

(19) Huang, D.; Lin, B.; Song, Y.; Guan, Z.; Cheng, J.; Zhu, Z.; Yang, C. J. Staining traditional colloidal gold test strips with Pt nanoshell enables quantitative point-of care testing with simple and portable pressure meter readout. *ACS Appl. Mater. Interfaces* **2019**, *11* (2), 1800-1806 https://doi.org/10.1021/acsami.8b15562.

(20) Li, J.; Liu, F.; Zhu, Z.; Liu, D.; Chen, X.; Song, Y.; Zhou, L.; Yang, C. In situ Pt staining method for simple, stable, and sensitive pressure-based bioassays. *ACS Appl. Mater. Interfaces* **2018**, *10* (16), 13390–13396. https://doi.org/10.1021/acsami.8b03567.

(21) Huang, Y.; Xu, T.; Wang, W.; Wen, Y.; Li, K.; Qian, L.; Zhang, X.; Liu, G. Lateral flow biosensors based on the use of micro- and nanomaterials: A review on recent developments. *Microchim. Acta* **2020**, *187* (1), # 70. https://doi.org/10.1007/s00604-019-3822-x.

(22) Yang, H.; Xu, W.; Zhou, Y. Signal amplification in immunoassays by using noble metal nanoparticles: a review. *Microchim. Acta* **2019**, *186* (12), # 859. https://doi.org/10.1007/s00604-019-3904-9.

(23) Vashist, S. K.; Venkatesh, A. G.; Marion Schneider, E.; Beaudoin, C.; Luppa, P. B.; Luong, J. H. T. Bioanalytical advances in assays for c-reactive protein. *Biotechnol. Adv.* **2016**, *34* (3), 272–290. https://doi.org/10.1016/j.biotechadv.2015.12.010.

(24) Gao, Z.; Shao, S.; Gao, W.; Tang, D.; Tang, D.; Zou, S.; Kim, M. J.; Xia, X. Morphology-invariant metallic nanoparticles with tunable plasmonic properties. *ACS Nano* **2021**, *15*, (2), 2428-2438. https://doi.org/10.1021/acsnano.0c06123.

(25) Anfossi, L.; Di Nardo, F.; Cavalera, S.; Giovannoli, C.; Baggiani, C. Multiplex lateral flow immunoassay: an overview of strategies towards high-throughput point-of-need testing. *Biosensors* **2018**, *9* (1), #2. https://doi.org/10.3390/bios9010002.

(26) Merkoçi, F.; Patarroyo, J.; Russo, L.; Piella, J.; Genç, A.; Arbiol, J.; Bastús, N. G.; Puntes, V. Understanding galvanic replacement reactions: the case of Pt and Ag. *Mater. Today Adv.* **2020**, *5*, # 100037. https://doi.org/10.1016/j.mtadv.2019.100037.

(27) Gao, Z.; Tang, D.; Tang, D.; Niessner, R.; Knopp, D. Target-induced nanocatalyst deactivation facilitated by core@shell nanostructures for signal-amplified headspace-colorimetric assay of dissolved hydrogen sulfide. *Anal. Chem.* **2015**, *87* (19), 10153–10160. https://doi.org/10.1021/acs.analchem.5b03008.

(28) González, E.; Merkoçi, F.; Arenal, R.; Arbiol, J.; Esteve, J.; Bastús, N. G.; Puntes, V. Enhanced reactivity of high-index surface platinum hollow nanocrystals. *J. Mater. Chem. A* **2015**, *4* (1), 200–208. https://doi.org/10.1039/c5ta07504a.

(29) Wu, J.; Wang, X.; Wang, Q.; Lou, Z.; Li, S.; Zhu, Y.; Qin, L.; Wei, H. Nanomaterials with enzyme-like characteristics (nanozymes): next-generation artificial enzymes (II). *Chem. Soc. Rev.* **2019**, *48* (4), 1004–1076. https://doi.org/10.1039/C8CS00457A.

(30) Jiang, B.; Duan, D.; Gao, L.; Zhou, M.; Fan, K.; Tang, Y.; Xi, J.; Bi, Y.; Tong, Z.; Gao, G. F.; Xie, N.; Tang, A.; Nie, G.; Liang, M.; Yan, X. Standardized assays for determining the catalytic activity and kinetics of peroxidase-like nanozymes. *Nat. Protoc.* **2018**, *13* (7), 1506–1520. https://doi.org/10.1038/s41596-018-0001-1.

(31) Panferov, V. G.; Safenkova, I. V.; Zherdev, A. V.; Dzantiev, B. B. Urchin peroxidase-mimicking Au@Pt nanoparticles as a label in lateral flow immunoassay: impact of nanoparticle composition on detection limit of *Clavibacter michiganensis*. *Microchim. Acta* **2020**, *187* (5), # 268. https://doi.org/10.1007/s00604-020-04253-3.

(32) Di Nardo, F.; Cavalera, S.; Baggiani, C.; Giovannoli, C.; Anfossi, L. Direct vs mediated coupling of antibodies to gold nanoparticles: the case of salivary cortisol detection by lateral flow immunoassay. *ACS Appl. Mater. Interfaces* **2019**, *11* (36), 32758–32768. https://doi.org/10.1021/acsami.9b11559.

(33) Loynachan, C. N.; Thomas, M. R.; Gray, E. R.; Richards, D. A.; Kim, J.; Miller, B. S.; Brookes, J. C.; Agarwal, S.; Chudasama, V.; McKendry, R. A.; Stevens, M. M. Platinum nanocatalyst amplification: redefining the gold standard for lateral flow immunoassays with ultrabroad dynamic range. *ACS Nano* **2018**, *12* (1), 279–288. https://doi.org/10.1021/acsnano.7b06229.

(34) Li, B.; Ge, L.; Lyu, P.; Chen, M.; Zhang, X.; Xie, S.; Wu, Q.; Kwok, H. F. Handheld pH meter – assisted immunoassay for C-reactive protein using glucose oxidase – conjugated dendrimer loaded with platinum nanozymes. *Microchim. Acta* **2021**, *188* (1), # 14. https://doi.org/10.1007/s00604-020-04687-9

(35) Boonkaew, S.; Chaiyo, S.; Jampasa, S.; Rengpipat, S.; Siangproh, W.; Chailapakul, O. An Origami paper-based electrochemical immunoassay for the C-reactive protein using a screen-printed carbon electrode modified with graphene and gold nanoparticles. *Microchim. Acta* **2019**, *186* (3), # 153. https://doi.org/10.1007/s00604-019-3245-8.

(36) Castelli, G. P.; Pognani, C.; Meisner, M.; Stuani, A.; Bellomi, D.; Sgarbi, L. Procalcitonin and C-reactive protein during systemic inflammatory response syndrome, sepsis and organ dysfunction. *Crit. care* **2004**, *8* (4), 234–242. https://doi.org/10.1186/cc2877.

(37) Jiang, B.; Fang, L.; Wu, K.; Yan, X.; Fan, K. Ferritins as natural and artificial nanozymes for theranostics. *Theranostics* **2020**, *10* (2), 687–706. https://doi.org/10.7150/thno.39827.